# Optimization of Sail Settings using RBF Mesh Morphing

**Mechanical Engineering Degree Thesis**

Enterprise Engineering Dept, University of Rome "Tor Vergata"

Academic Year 2012/2013

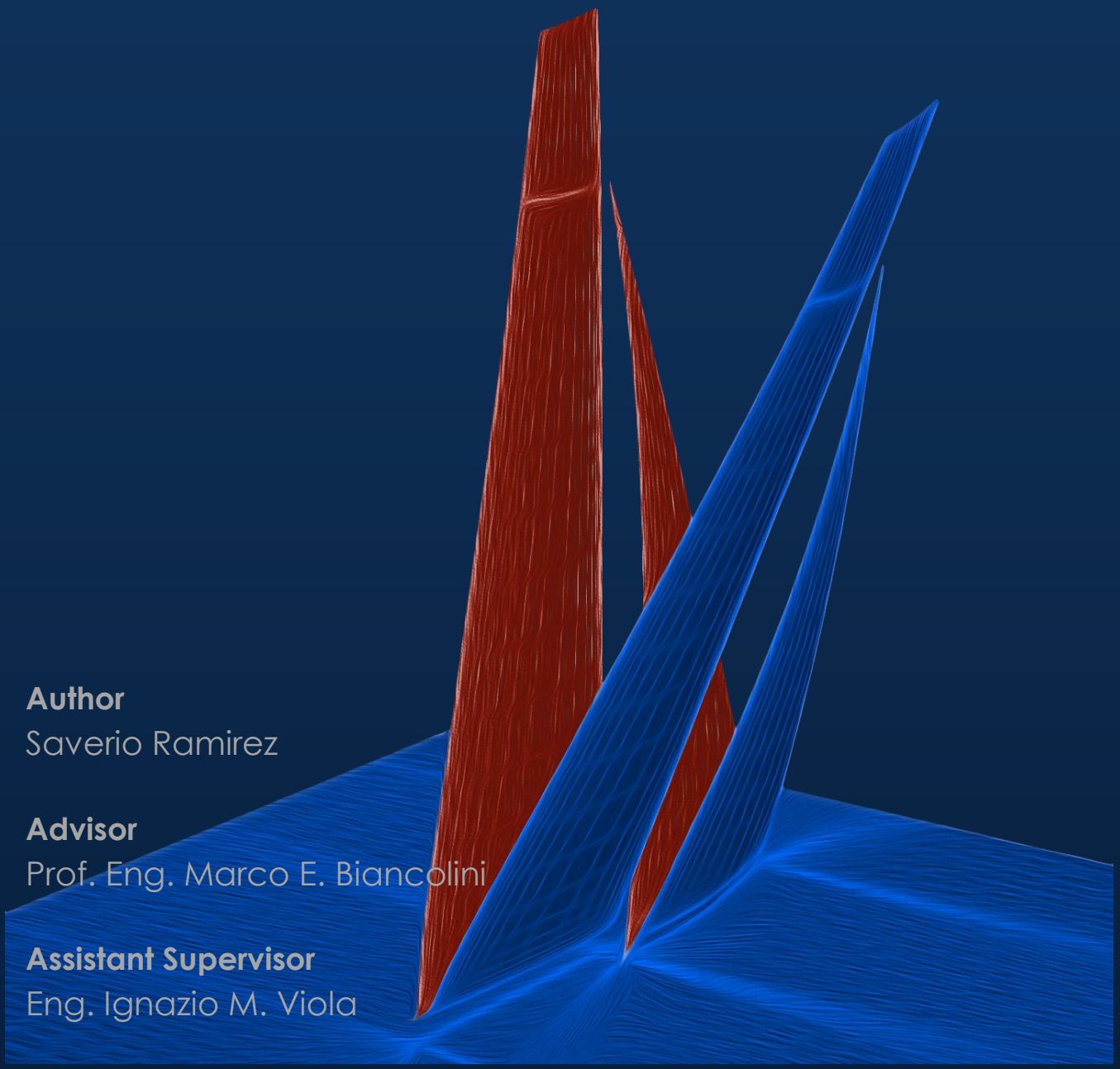


**Author**
Saverio Ramirez

**Advisor**
Prof. Eng. Marco E. Biancolini

**Assistant Supervisor**
Eng. Ignazio M. Viola

# Table of Contents

# Abstract

The purpose of this project is to outline the most recent results obtained thanks to the ongoing cooperation between the University of Rome "Tor Vergata" and the Yacht & Superyacht Research Group of the University of Edinburgh. The object of this joint project is to study the use of *mesh morphing* within the sailing world and has involved research staff, professors and students from both centres.

*Mesh morphing* allows users to modify the mesh of the fluid dynamic vessel model in a quick and effective way; these modifications may be applied to the shape of the components and to their position. This method is therefore useful both during the design phase, in order to optimize surface shapes, and in the set-up phase, allowing the user to modify the sails' adjustment and the vessel's layout.

The accuracy of the *CFD* model in relation to the experimental reference model has been proven in the past thanks to extensive wind-tunnel testing focused on the evaluation of the effects caused by trimming two sail-setting parameters: the *mainsail sheeting angle* and the *genoa sheeting angle*, implemented on the virtual model using the standard *remeshing* method. The correlation between calculations and experimental data is demonstrably high, both in terms of overall force and of pressure distributions. *Mesh morphing* was then used to elaborate the same geometric parameters. The CFD model made parametric this way has then proven to be so reliable, accurate and computationally low-cost as to extend the geometry exploration to other two significant parameters in a sailing boat: the *apparent wind angle* and the *heeling angle*.

The study of these four sail-setting parameters is the focus of this thesis. This includes the elaboration of *mesh morphing* of the original baseline mesh; the *DOE* set-up for the *CFD* runs and the runs themselves; the generation of the response surfaces; the sensitivity analysis and the optimization research based on these; and finally the *CFD* re-computation and post-processing on the mesh morphed with the optimal settings thus found.

# Nomenclature

| | |
|---|---|
| $F_A$ | *Product of the Aerodynamic Force* |
| $F_X$ | *Driving force* |
| $F_Y$ | *Side force* |
| $F_D$ | *Drag force* |
| $F_L$ | *Lift force* |
| $C_p$ | *Pressure Coefficient* |
| $C_x$ | *Propulsive thrust coefficient* |
| $C_y$ | *Transverse thrust coefficient* |
| $C_d$ | *Drag coefficient (or drag)* |
| $C_l$ | *Lift coefficient (or lift)* |
| $G$ | *Genoa Sheeting Angle (G1=0°, G2=1.5°, G3=2.9°, G4=4.1°)* |
| $h$ | *Generic polynomial* |
| $M$ | *Mainsail Sheeting Angle (M1=0°, M2=1°, M3=2°, M4=3°)* |
| $n$ | *Generic space dimensions* |
| $N$ | *Number of RBF centres* |
| $q$ | *Generic polynomial* |
| $r$ | *Distance between 2 points* |
| $Re$ | *Reynolds' number* |
| $s$ | *Interpolation function composed of one RBF and one polynomial* |
| $s_x, s_y, s_z$ | *Morphing field components* |
| $\boldsymbol{g}$ | *vector of the scalar function to be interpolated, relative to the RBF centres* |
| $\boldsymbol{x}$ | *Position vector in the Cartesian system O (x,y,z)* |
| $\hat{\boldsymbol{x}}$ | *RBF centres vector* |

| | |
|---|---|
| $\boldsymbol{M}$ | *Interpolation matrix used for the RBF structure* |
| $\boldsymbol{P}$ | *Limitation matrix used for the RBF structure* |
| $\varphi$ | *Radial base function* |
| $\boldsymbol{\beta}$ | *Coefficients of the structural polynomial vector* |
| $\boldsymbol{\gamma}$ | *Coefficients of the structural RBF vector* |
| *Fr* | *Froude number* |
| *g* | *gravity acceleration* |
| *u* | *boat speed* |
| *l* | *waterline length* |
| *dp* | *design point* |
| *CG* | *Center of Gravity* |
| *AWA* | *Apparent Wind Angle* |
| *CFD* | *Computational Fluid Dynamics* |
| *DOE* | *Design of Experiments* |
| *FEM* | *Finite Element Model* |
| *OSF* | *Optimal Space Filling* |
| *RBF* | *Radial Basis Functions* |
| *V&V* | *Verification and Validation* |
| *VMG* | *Velocity Made Good* |
| *VPP* | *Velocity Prediction Program* |
| *RANS* | *Reynolds-Averaged Navier-Stokes* |

# 1. Introduction

## 1.1. Terminology and Principles of Sail Aerodynamics

Sailing may be divided into two main categories, depending on the wind direction as it strikes the vessel: upwind and downwind.

In so-called upwind conditions, which will be the main focus of this study, the angle between the real wind direction and the vessel's longitudinal axis falls approximately between 35° and 70°. The angle between the apparent wind direction and the vessel's heading, conversely, falls between 17° and 45°.

Figure 1 shows the basic nautical lexicon applied to a sport-cruiser sailing boat.

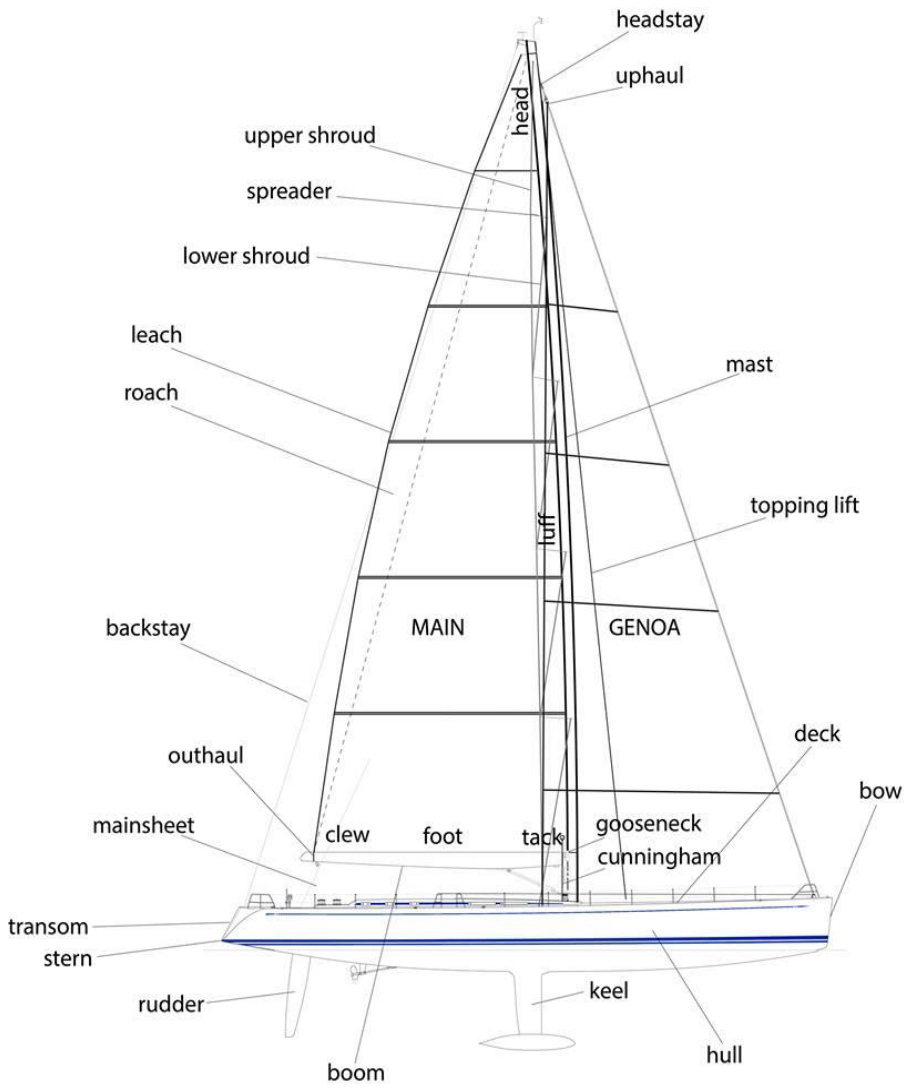


*Figure 1. Drawing of a Swan 80 FD, © Nautor Holding.*

Modern sailing vessels equipped with a fore-and-aft rig (first used regularly outside of coastal waters from the late 19th Century onwards) are able to sail upwind thanks to their sails' modern design. These are designed in order to be set very tight to the boat and generate high *lift force* and reduced *drag force*. By definition, the lift is perpendicular to the wind direction and the drag is parallel to it. The projection of the result of these on the longitudinal axis of the vessel is what is known as the *driving force*, which propels the vessel forward. The projection on the transversal axis, conversely, is defined as *side force*, which is balanced by the hull's transversal area and makes the boat heel leeward.
Modern racing vessels, on occasion, can travel at such speeds that, despite the fact they are sailing downwind, their rig is experiencing upwind conditions, because of the relative high vessel speed compared to the wind speed, which generates a low

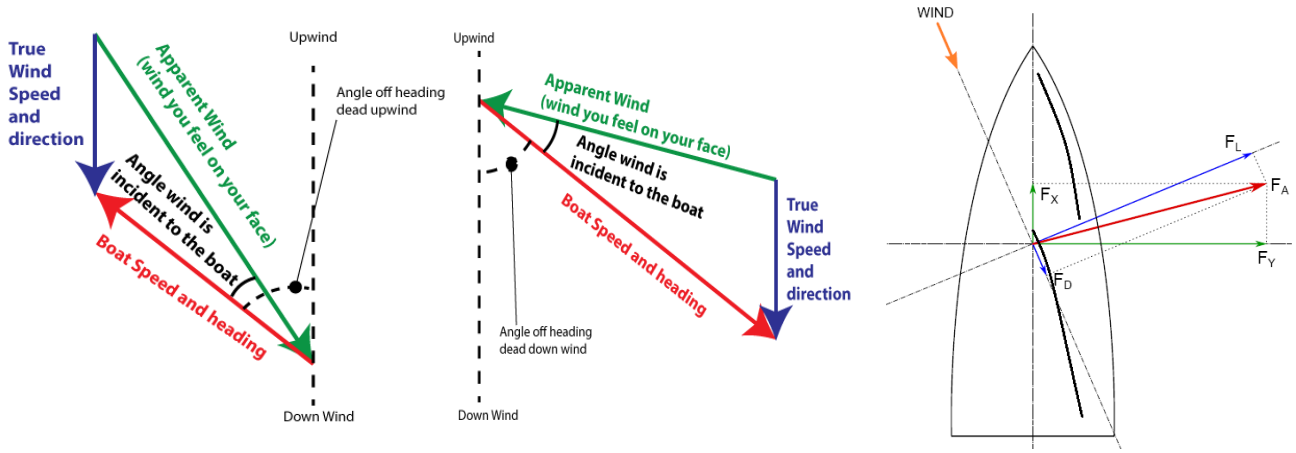


*Figure 2. Vector diagrams of wind speed, vessel speed and aero dynamical forces.*

*apparent wind angle,* albeit with a high *real wind angle.* For this reason modern sailing craft use sailing rigs that are largely (if not completely) upwind-type. This is made clear by Figure 2, where the vector diagram of wind and vessel speed is shown (both in upwind and downwind*)*, as well as the vector diagram of the aero-forces.

The America's cup, which represents the pinnacle of technology applied to professional sailing, was raced, in the edition concluded some months ago, with AC72 Class boats (Figure 3). These are *foiling* multi-hulls equipped with a rigid thick wing-type Mainsail, a small flexible Genoa and a flexible, slim Code 0, used only in very light wind conditions. This class of vessel is capable of speeds up to almost 50 kts and a *VMG* much higher than the wind speed, so they sail exclusively in conditions where the *AWA* falls between 17° and 35° (strictly upwind sailing conditions).

## 1.2. Technical Specifications of Racing Sails


*Figure 3. The Italian Challenge for the 33rd America's Cup, Luna Rossa. (July 2013, San Francisco, USA - © Luna Rossa Challenge)*

Racing sails are designed to obtain the best possible performance. In wind conditions up to "moderate", this result is obtained by maximising the component of direct aerodynamic force as applied to the heading. With stronger winds, the optimization is also dependent on the hydrostatic and hydrodynamic characteristics of the vessel.

Sails are thin multi-slotted wings, with relatively small *aspect ratio*, using very thin airfoil sections and operating at low *Reynolds number*. Typically the rig contains two sails set fore-and-aft with *aspect ratio* between two and three and the sailcloth thickness of less than 1% of the chord and a *Re* to the order of 10^5 in relation to the aerodynamic chord. Given the slight extension and the relatively low *Re*, the current sails are to be considered very efficient in aerodynamic terms. In fact, sails can allow lift/drag ratio higher than 13 and maximum lift higher than 3.5 (Viola & Flay, 2011). The efficiency of sails is due to complex flow features that are specific of airfoils with sharp leading edge and operating at low Re.

The genoa is the standard foresail employed in medium-light wind conditions when sailing close to the wind. Its main characteristic is an acute leading edge relative to the chord (with a radius of less than 1% of the chord) which leads to a laminar separation of the flow in correspondence to the depressed side). Transition occurs in the separated shear layer leading to reattachment in the first quarter of the sails, forming the so-called laminar separation bubble associated with a suction peak near the leading edge. Downstream a turbulent boundary layer develops. The sail camber leads

to a suction peak around mid chord and thus to a high adverse pressure gradient which leads to trailing edge separation. On the windward (pressure) side, the velocity and pressure gradients are small and a boundary layer develops along the chord.

The mainsail is the aft sail and it is used in almost any sailing conditions. Differently from the foresail, the leading edge of the mainsail is attached to the mast, which has an elliptical shape with radii of the order of 10% of the chord. *Re* based on the mast diameter is of the order of 104, leading the laminar boundary layer to separate from the mast and reattach on the sail after the laminar-to-turbulent transition. The pressure distributions on the mainsail are similar to those on the genoa, though the mainsail experiences the downwash of the foresails, while the foresail experiences the upwash of the mainsail. Therefore, the mainsail shows smoother pressure distributions while the foresail shows higher suction peaks.

Figure 4 shows a schematic of the flow around mainsail and genoa while sailing close to the wind and around the gennaker (bow sail for downwind sailing points) and mainsail while sailing on a close reach.

## 1.3. Background of Numerical Modelling of Sails

Numerical simulation has become a key element in sail design since the 70s, when potential flow codes (such as Milgram 1968a and 1968b) first came to prominence. The potential flow method, however, does not allow the laminar separation bubble to be simulated and thus does not guarantee a sufficient degree of accuracy. The first *RANS* simulation on sails designed for navigation close to the wind was undertaken by Miyata and Lee (Miyata & Lee, 1999) and represented a major breakthrough in simulation accuracy in this sector, as it allowed users to take into account viscous effects. However, these early calculations overestimated the drive force by approximately 28% and underestimated lateral force by approximately 18% when measuring data in a wind-gallery, probably due to the size of the mesh, which was inadequate to correctly represent the area of action. Recently, there has been a significant growth in the number of calculation resources available for *CFD* analysis and many authors have proven that it is possible to obtain very accurate CFD analyses in terms of total force in this sector, in line with experimental data (see Yoo & Kim, 2006; Ciortan & Soares, 2007; Masuyama *et al,* 2007).

In 2012, experiments were carried out on rigid sails with acquisition of pressure along their profiles (Viola et al, 2012). Thanks to these experiments it has been possible to demonstrate how trimming the sails influences the distribution of pressure and how it is possible to refine and validate the CFD model based on local rather than global quantities.

The sailing industry still uses methods based on potential flows during the design phase, due to the low cost of calculations and the ease in generating a new configuration, features which allow for the analysis of a large number of settings. Every chosen arrangement must be evaluated in order to establish its potential under various operating conditions, and each operating condition requires the establishment of an optimal sheeting angle, which is specific to the chosen arrangement. The adjustment of the sails is chiefly dependent on the positioning of the lines, on the twist angles and, to a lesser extent, on the depth of the chord and the curvature, as well as on other, less influential parameters. The requirements of the industrial apparatus are moving towards greater accuracy and thus, bearing in mind the vast calculation power available, towards workflows completely based on *RANS* analysis rather than potential flows. One of the major obstacles in this regard is the long preparation time required for the creation of a reliable *CFD* model for a single arrangement; typically the workflow leading from the *CAD* model to the *CFD* is made up of several distinct phases (surface mesh, volume mesh, contour conditions, solver setup) and is so complex as to render parametric analysis which would allow for the exploration of a number of variants of the base arrangement impractical.

*Mesh morphing* is quickly becoming the preferred solution as an instrument for the creation of a parametric *CFD* model. The new shapes are obtained from the base one by deforming the mesh, that is by changing the position of the nodes. This technique is usually more speedy than remeshing, and also allows the preservation of the same topology. If the distortions are not significant enough to affect the quality of the calculations, having a consistent mesh can be a source of numerous advantages, such as: the possibility of initialising the calculation with flow conditions already resolved for the baseline (thus significantly reducing the convergence time), the elimination of remeshing noise (no matter how controlled, a small dependency on the mesh's result is always present), and the use of an evolutionary methodology (fluid-structure interaction).

There are several different *mesh morphing* methods for large scale meshes. The first technique to gain a foothold in industrial use is *Free Form Deformation* (Sedrberg, 1986) in which volumes of control are modified utilising Bernstein polynomials. This is a *meshless* method which works very well on partitioned meshes and those with hybrid elements. Although this method allows the creation of very interesting new shapes, it lacks accuracy as the box points of control are not located on the surfaces, the movement of which cannot therefore be directly controlled. Accuracy is easily obtained with *mesh morphing* methods based on the mesh itself, such as the pseudosolid method (Masud, 2007), wherein a *FEM* solution is controlled in order to propagate the movement imposed on the surfaces within the volume. Methods based on the mesh have the disadvantage of having to support all the complexities of the original mesh (which is typically partitioned and hybrid). A good compromise between these two approaches is the *Radial Basis Functions* method, which combines the benefits of a *meshless* model with a high degree of accuracy. In this case, the *RBF* morphing field is outlined by defining a cloud of points within the space; the known movement in any point of the cloud is interpolated exactly in the control points and extrapolated in a very delicate manner throughout the whole space. Despite the fact that some very interesting studies have been published proving how this technique may be used for the deformation of *CFD* meshes (Jakobsson, 2007; de Boer, 2007), the high cost of *RBF* has limited its wider use in the past (the cost of a direct solution increases by N^3 where *N* is the number of *RBF* points). More recently, studies have been published for use of this method with large-scale datasets. Rendall & Allen (2009, 2010) have implemented and optimised a greedy method which enables us to reach the desired accuracy using only a small subset of the original cloud (controlling the ensuing error); the effectiveness of their approach has been proven in its ability to reproduce shapes and ways of tacking to a high elevation obtained with FEA analysis. Estruch *et al* (2012) have presented a parallel implementation capable of working with large-scale meshes.

The first industrial solution based on *RBF mesh morphing* was introduced in 2009. This was the RBF Morph™ software (Biancolini et al, 2009) which possesses a high performance RBF solver which scales as *N^1.6*. An exhaustive description of this tool is available in (Biancolini, 2012). Some relevant examples are given in Caridi & Wade (2012), Cella & Biancolini (2012) and Khondge & Sovani (2012).

## 1.4. The Theory of *Radial Basis Functions*

In this study, *RBFs* are used to produce a solution in terms of movements upon the mesh, starting from a series of source points within which the movement is known. This approach is effective both for the modelling of the surface mesh's profiles and for smoothing the volume mesh. The same method is then utilised in the generic *n*-dimensional space and thus used as an effective interpolation instrument for the evaluation of response surfaces.

*RBF*s are a very powerful tool developed for the interpolation of series of scattered and disorganised data; they are capable of interpolating a function defined on distinct points anywhere within the space guaranteeing an exact value for said points. The behaviour of the function within the space between the points depends on the type of *RBF* chosen. *RBF*s are characterized by a compact or global support; some functions require a polynomial-type correction.

Table 1 shows the typical *RBFs* with global and compact support. It is worth noting that *RBF*s are scalar functions with a variable scalar *r,* which represents the Euclidean distance between 2 points within the *n*-dimensional space (*n = 2,3* for *mesh morphing* applications).

| **Radial Basis Functions with global support** | $\varphi(r)$ |
|---|---|
| Spline type ($R_n$) | $r^n, n\ odd$ |
| Thin plate spline ($TPS_n$) | $r^n \log(r), n\ even$ |
| Multiquadric (MQ) | $\sqrt{1+r^2}$ |
| Inverse multiquadric (IMQ) | $\frac{1}{\sqrt{1+r^2}}$ |
| Inverse quadratic (IQ) | $\frac{1}{1+r^2}$ |
| Gaussian (GS) | $e^{-r^2}$ |
| **Radial Basis Functions (*RBF*) with compact support** | $\varphi(r) = f(\xi), \xi \leq 1, \xi = \frac{r}{R_{sup}}$ |
| Wendland $C^0$ (C0) | $(1-\xi)^2$ |
| Wendland $C^2$ (C2) | $(1-\xi)^4(4\xi+1)$ |
| Wendland $C^4$ (C4) | $(1-\xi)^6\left(\frac{35}{3}\xi^2+6\xi+1\right)$ |

*Table 1. Typical RBFs with global and compact support*

As will be illustrated in detail, it is necessary to solve a system of linear equations in order to calculate the constants. Once the unknown constants have been found, the movement of an arbitrary point within or without the domain (interpolation/extrapolation) equals the sum of the radial contribution of every source point (if the point falls within the domain of influence).

The details of this theory are illustrated utilising some equations. An interpolation function made up of *RBF* $\varphi$ and a polynomial *h* is defined as follows:

$$s(\boldsymbol{x}) = \sum_{i=1}^{N} \gamma_i \varphi(\|\boldsymbol{x} - \hat{\boldsymbol{x}}_i\|) + h(\boldsymbol{x}) \tag{1}$$

Where $\hat{x}$ is the position of the *N* centres.

The degree of the polynomial has to be chosen depending on the kind of RBF adopted. A radial basis fit exists if the coefficients $\gamma_i$ and the weights of the polynomial can be found such that the desired function values are obtained at source points and the polynomial terms gives no contributions at source points, that is:

$$s(\hat{\boldsymbol{x}}_{\boldsymbol{i}}) = \boldsymbol{g}_i, 1 \leq i \leq N \tag{2}$$

$$\sum_{i=1}^{N} \gamma_i q(\hat{\boldsymbol{x}}_{\boldsymbol{i}}) = 0 \tag{3}$$

for all polynomials q with a degree less or equal to that of polynomial *h*. The minimum degree of the polynomial *h* depends on the choice of *RBF.* In the case where the system is defined, there is a single solution. If the *RBF*s have been defined as strictly positive to the order of *m < 2*, it is possible then to utilise a linear polynomial of the type:

$$h(\boldsymbol{x}) = \beta_1 + \beta_2 x + \beta_3 y + \beta_4 z \tag{4}$$

The following exposition will assume said hypothesis is valid. One of the consequences of utilising a linear polynomial is that rigid translations are represented in an exact fashion. The values for the *y* coefficients of the *RBF*s and the $\gamma_i$ coefficients of the linear polynomial may be obtained by solving the linear system (order of N+4):

$$\begin{pmatrix} \boldsymbol{M} & \boldsymbol{P} \\ \boldsymbol{P^T} & \boldsymbol{0} \end{pmatrix} \begin{pmatrix} \boldsymbol{\gamma} \\ \boldsymbol{\beta} \end{pmatrix} = \begin{pmatrix} \boldsymbol{g} \\ \boldsymbol{0} \end{pmatrix} \tag{5}$$

Where ***g*** are the known values at the source points and ***M*** is the matrix of interpolation defined by calculating all the radial interactions between the source points:

$$M_{ij} = \varphi\left(\left\|\hat{\boldsymbol{x}}_{\boldsymbol{i}} - \hat{\boldsymbol{x}}_{\boldsymbol{j}}\right\|\right), 1 \leq i \leq N, 1 \leq j \leq N \tag{6}$$

And ***P*** (eq. 7) is the constraint matrix which contains a column of *1* and the positions *x y z* of the source points in the other columns; the control points selected cannot be contained within the same plane, otherwise the interpolation matrix will be singular.

$$\boldsymbol{P} = \begin{pmatrix} 1 & \hat{\boldsymbol{x}}_{\boldsymbol{1}} & \hat{\boldsymbol{y}}_{\boldsymbol{1}} & \hat{\boldsymbol{z}}_{\boldsymbol{1}} \\ 1 & \hat{\boldsymbol{x}}_{\boldsymbol{2}} & \hat{\boldsymbol{y}}_{\boldsymbol{2}} & \hat{\boldsymbol{z}}_{\boldsymbol{2}} \\ \vdots & \vdots & \vdots & \vdots \\ 1 & \hat{\boldsymbol{x}}_{\boldsymbol{N}} & \hat{\boldsymbol{y}}_{\boldsymbol{N}} & \hat{\boldsymbol{z}}_{\boldsymbol{N}} \end{pmatrix} \tag{7}$$

As far as concerns the issue of the volume smoothing, each component within the known field of movement of the source points will be interpolated as follows:

$$\begin{cases} s_x(\boldsymbol{x}) = \sum_{i=1}^{N} \gamma_i^x \varphi(\|\boldsymbol{x} - \hat{\boldsymbol{x}}_{\boldsymbol{i}}\|) + \beta_1^x + \beta_2^x x + \beta_3^x y + \beta_4^x z \\ s_y(\boldsymbol{x}) = \sum_{i=1}^{N} \gamma_i^y \varphi(\|\boldsymbol{x} - \hat{\boldsymbol{x}}_{\boldsymbol{i}}\|) + \beta_1^y + \beta_2^y x + \beta_3^y y + \beta_4^y z \\ s_z(\boldsymbol{x}) = \sum_{i=1}^{N} \gamma_i^z \varphi(\|\boldsymbol{x} - \hat{\boldsymbol{x}}_{\boldsymbol{i}}\|) + \beta_1^z + \beta_2^z x + \beta_3^z y + \beta_4^z z \end{cases} \tag{8}$$

The *RBF* method has several advantages which make it very interesting for use in *mesh morphing.* The key point is that, since it is a *meshless* method, the points on the grid are moved independently of what elements are connected to them, thus making it suitable for the parallel implementation. Once known, the solution is available in the memory of each calculation node of the group, and each partition has the possibility of moving its nodes independently of the others. Additionally, despite its *meshless* nature, the method is capable of controlling in an exact fashion the known deformations on the surface of the mesh; this effect is obtained by utilising all the nodes of the mesh as *RBF* centres.

It is interesting to note that the *RBFs* themselves can be used to interpolate scalar functions in a generic *n*-dimensional space and it has been proven that they represent an excellent instrument for the evaluation of meta-models and response surfaces (Jin *et al,* 2001).

In this study we have utilised a direct method for *DOE* post-elaboration (Lapack solver included in Mathcad software suite), with the *RBF* $\varphi(r) = r^3$. For *mesh morphing*, the RBF Morph™ rapid solver utilising a bi-harmonic $\varphi(r) = r$. nucleus was used. It is possible to find numerous examples in the literature of the *RBF* approach producing more than satisfactory reports. See chiefly "Partition of Unity Method" (Wendland, 2002), and "Fast Multipole Method" (Beatson, 2007).

# 2. Method

## 2.1. Outline

Within this thesis we present a method for the optimization of sail settings adjustments on a racing vessel heading upwind utilising *CFD RANS* simulations and the *RBF* method for *mesh morphing*. First of all, we introduce the *CFD* model based on an experimental model structure, proving its accuracy compared to the available experimental data. We then move on to a description of the algorithm utilised for *mesh morphing* considering both the base theory of *RBF* and the practical problem of placing the *RBF* points for the set-up of form modifications of interest for the proposed study, that is the *sail sheeting angles*, the *heeling angle* and the *apparent wind angle*.

Subsequently we explain how a 16-point *DOE* table, where the 4 input parameters are manually sorted into 4 values while the others remain null, is used to run a primary *CFD* analysis with low time expenditure, and is thus able to evaluate the effective verisimilitude of the overall model. Following this, we detail how the method based on algorithms of *optimal space filling* is utilised to generate a 100-point *DOE* where all the input parameters are blended together in order to obtain a substantial set of output points once the *CFD* calculation is performed.

In the final step, we show how *RBFs* are then used once again to compute an interpolation process on the output scattered data obtained as described above and generate high-density response surfaces where it is possible to evaluate the progress of the force with a very high degree of accuracy.

## 2.2. The *CFD* Model

The optimization of the adjustments is based on two key elements: a *CFD* parametric model and a tool capable of guiding said parametric model towards an optimal objective. Within this study, *RBFs* was used both to make the shape of the mesh parametric via the use of *mesh morphing* algorithms, and for the optimization phase as an interpolation instrument within the space of the form parameters.

The starting point is given as a CFD model whose accuracy has been verified when compared to the experimental evidence. Than to *mesh morphing* techniques this model thus becomes parametric, that is capable of altering its shape in a continuous fashion based upon the desired entry parameters, that is the *sheeting angle of mainsail and genoa,* the *AWA* and the *heeling angle.*

The *CFD* model reproduces a layout studied experimentally (Viola *et al,* 2011). Specifically, the rigid models of mainsail and genoa from an AC33-Class (used in the 2007 America's Cup) were studied, this being the object of experimentation at the

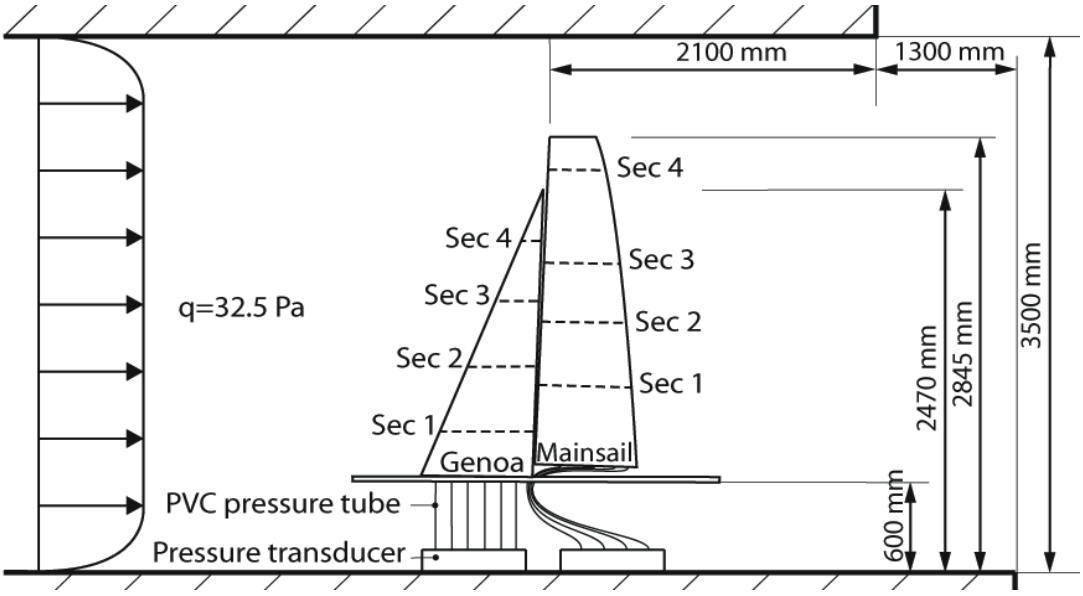


*Figure 5. Representation of the experimental model.*

University of Auckland's wind-tunnel. This (Figure 5) is an open gallery with a proofing section 7 meters wide by 3.5 tall; the floor and the ceiling extend for 5.1 m and 4.8 m downwind of the exit section respectively. The sails were fixed using lines unaffected by the flow 2.7 m downwind of the exit section. The relative position of the sails is such that it thus represents conditions encountered when the vessel is vertical and *AWA* = 19°. Mast and hull are not present in the model, the hull being replaced by a layer of wooden planking, to represent both the hull and the water surface. The pressure was measured in four horizontal sections on the genoa and mainsail. The test was based on evaluating the effects of the modification of two setting parameters, in a range of four values each: the *genoa sheeting angle* (G1-4) and the *mainsail sheeting angle* (M1-4), rotating the sails along the axes defined by the furthest attachment points at intervals of 1.4° and 1° respectively (genoa angle 0, 1.4°, 2.7°, 4.1° labelled as G1, G2, G3 and G4 and mainsail angle 0, 1°, 2°, 3° labelled as M1, M2, M3 and M4). For a total of 16 trim combinations.

The experimental setup was modelled with CFD analysis utilising a hexahedral structured mesh made up of 1,443,840 cells previously generated with ANSYS ICEM and solved with ANSYS Fluent®. The steady, incompressible *RANS* Newtonian problem was approached with a solver based on pressure and finite volumes. The turbulence was represented with $k-\epsilon$ SST adjusted for low *Re*. The grid allows us to maintain $y^+ < 3$ in the depression areas where a separation occurs and $5 < y^+ < 25$ on the upwind side, where the boundary layer remains attached. The grid is shown in Figure 3. The combination of speed and pressure occurs with a SIMPLEC schematic. Second order schematics were used as the third one showed difficulty to converge.

The *CFD* simulations were verified and validated using experimental data from wind-tunnel testing (Viola *et al*, 2011). A good concurrence was found to exist between the pressure distributions measured in numerical and experimental methodologies in all 16 base settings tested. Each setting was obtained via a standard *re*mesh*ing* approach. For example, Figure 6 shows the pressure coefficient $C_p$ measured experimentally and calculated numerically for setting G3M2. The main difference between the experimental and numerical data is to be found near the hoist (leading edge) on both sides, upwind (pressure) and downwind (de-pressure). Realistically the differences recorded on the upwind side are due to the fact that the virtual model is made up of sails with a nil thickness, while the experimental one possessed a thickness equivalent

to approximately 1% of the sail chord and was linked at approximately 20% to produce a sufficiently acute hoist. As far as concerns the downwind side, it is believed that the differences recorded in the upper sections of mainsail and genoa are due to the relative geometric imprecision which produces slight differences in shape at the local angle of attack. Indeed, when the angle of attack is of a value close to the ideal, small variations in such lead to sizeable changes in the suction peak at the leading edge. Similarities and differences of this nature were also recorded for the base settings with other values of sheeting angles.

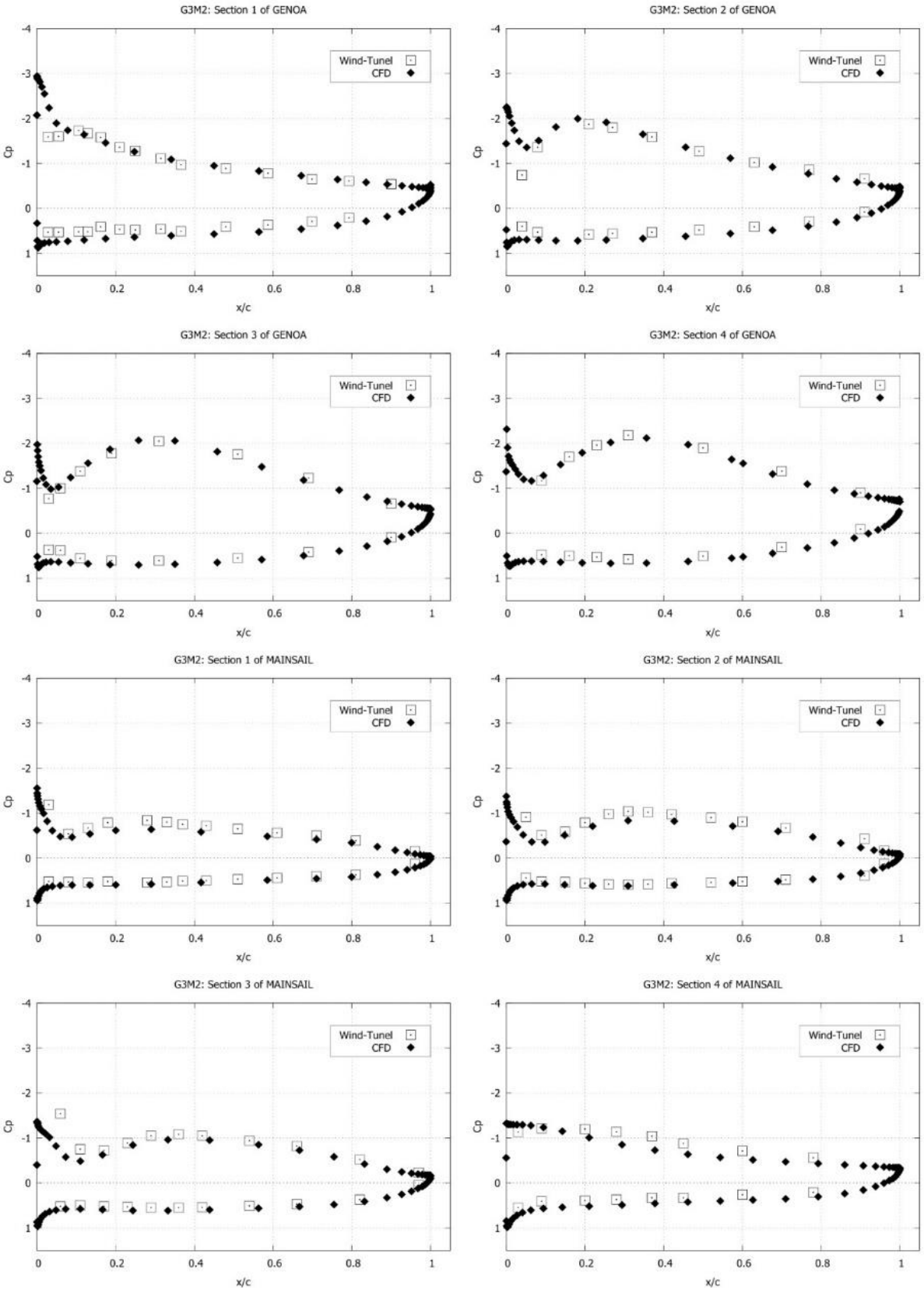


*Figure 6. Pressure coefficient measured in experimental and computational fashion on genoa (left) and mainsail (right).*

## 2.3. *Mesh Morphing* Elaboration

RBF Morph™ software, which consists in a set of libraries to install in ANSYS Fluent® environment, was used to configure all four of the modification parameters for the previously mentioned trim settings.

In this study we refer to a baseline configuration of the virtual model characterised by a sheet trim of G1M1, in which the sails are fully winched tight, 19° AWA and a null heeling angle (see section 2.2 – The *CFD* Model for details). The morphing amplification units relative to the parameters discussed below were made equal to a 1° modification of the parameter in question, so as to render the input values expressed in amplification units numerically equivalent to the degree of rotation. Positive values for these parameters represent, in this order: sail easing, bearing away, and leeward heeling.

The set-up for the parameters related to the sheeting angles of the mainsail and genoa are very similar, since this is essentially the same type of adjustment applied to two different sails, which differ in terms of their shape and the way in which said adjustment is applied. In light of this similarity, the two setups will be dealt with concurrently below. To follow, the setups referring to the *AWA* and the *heeling angle* will be discussed.

### *mainsail and genoa sheeting angles*

Two *surface sets* are defined, that is a grouping of the nodes contained within the portion of surface selected. The nodes extracted from the relevant surface are utilised as *RBF* centres to accurately control the shape of the sails thus assigning a rigid rotation along the axis of a sail keeping the points belonging to the other unaltered (Figure 7). It is important to note that the software integrates a non-linear amplification algorithm that allows us to amplify the rotation without the need to regenerate the *RBF* structure.

the overall problem is composed in this case of 4156 centres and requires approximately 4s for the *RBF* solution fit. The shape modifiers thus obtained are then verified with the preview tools. We have used a combination of both modifiers at maximum values (e.g. 4° for the *sheeting angle of the genoa* and 4° for the *mainsail sheeting angle*) so as to observe the effects on the surface mesh*;* contextually, the original mesh is also presented to evidence the effect of the shape variation (Figure 8).

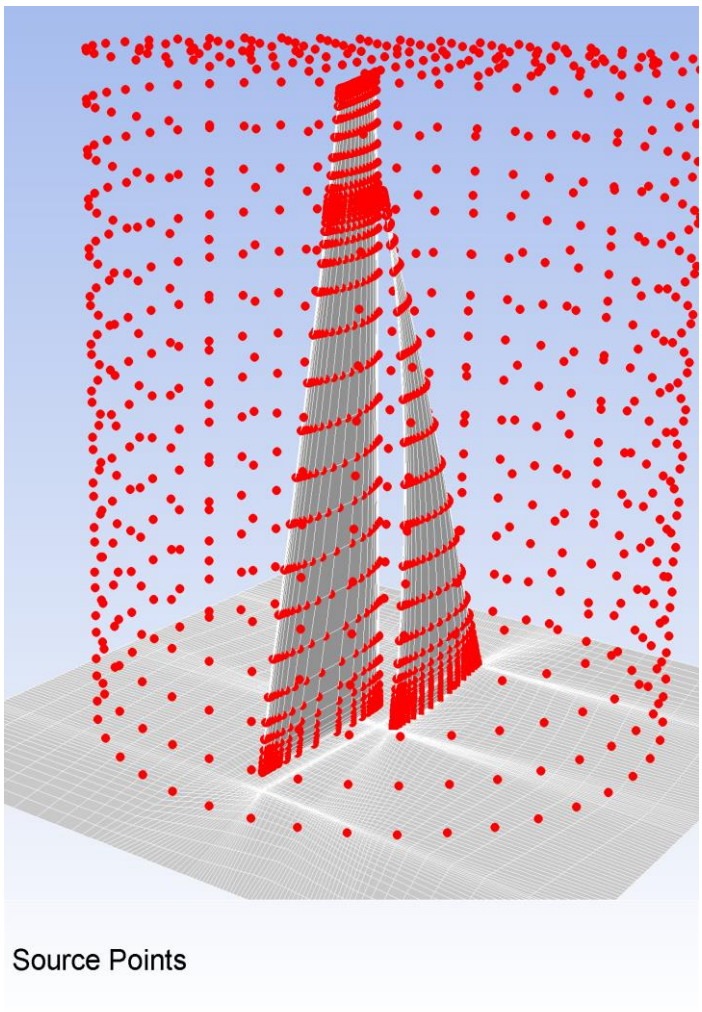


*Figure 7. Source points of the surface sets.*

The effect of the shape modifiers at maximum height (acting separately, see Figure 9) is evidenced in the section *y = 1 m*. The original and deformed mesh*es* are overlaid utilising an overhead orthographic view.

The result of analysis of the deformed grids showed that, within the interval of interest, the quality is very well preserved (see Table 2).

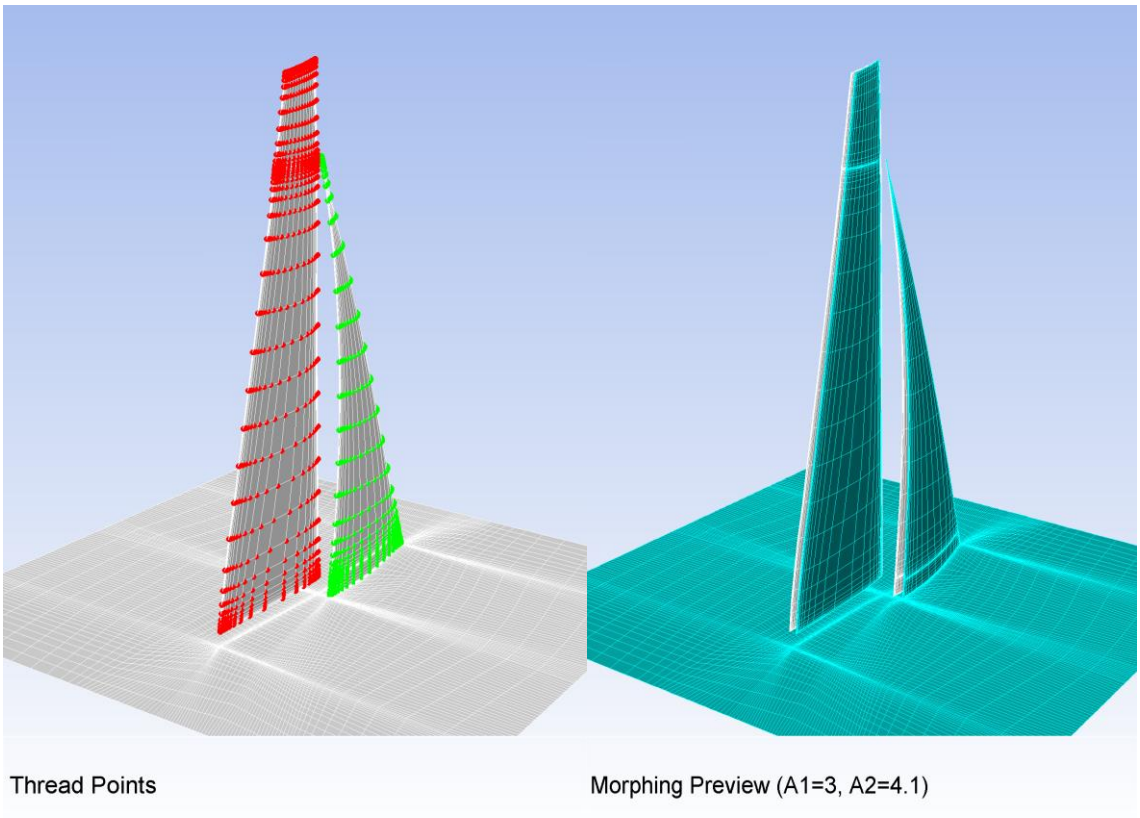


*Figure 8. Thread points (left) and morphing preview set with the amplification values above (right).*

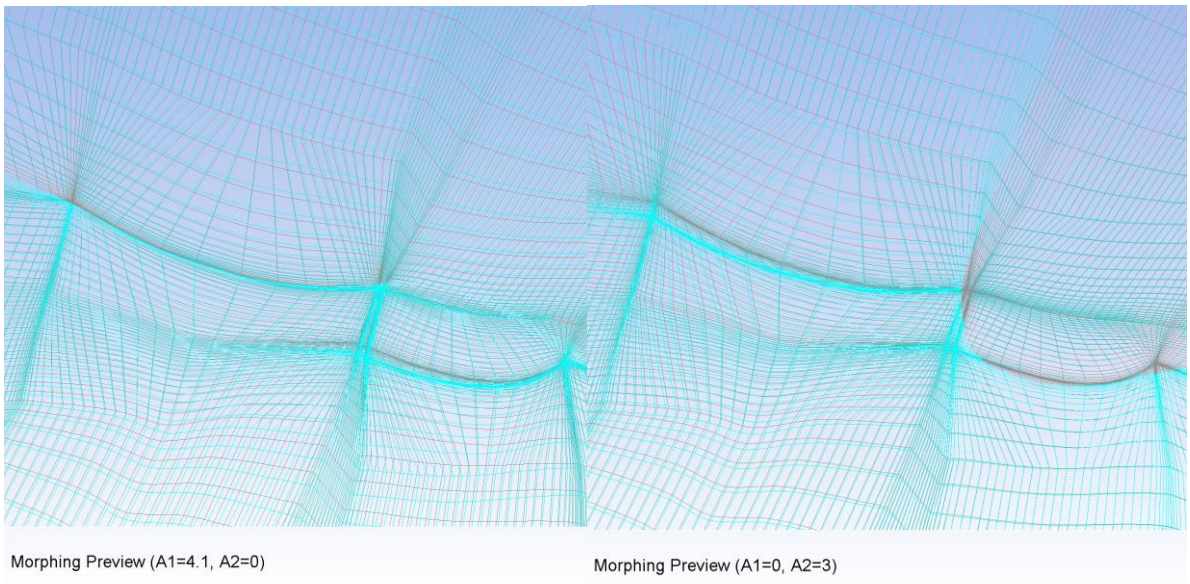


*Figure 9. Morphing actions set with amplifications values above evidenced at y=1 m.*

| ***genoa sheeting angle morphing amplification*** | ***mainsail sheeting angle morphing amplification*** | ***minimum orthogonal quality*** | ***maximum aspect ratio*** |
|---|---|---|---|
| *0* | *0* | *1.64e-02* | *1.555e+03* |
| *5* | *0* | *1.38e-02* | *1.539e+03* |
| *0* | *5* | *1.63e-02* | *1.549e+03* |
| *5* | *5* | *1.41e-02* | *1.539e+03* |

*Table 2. Quality of the deformed meshes calculated at the extreme ends of the validity ranges for sail angles (1 amplification unit = 1° deformation on the baseline).*

### *apparent wind angle*

As far as the *AWA* setup is concerned, it has been decided to adopt two *cylindrical encaps* with a spacing of 0.2 m to distribute 3300 *RBF* points on the cylinders. This technique is rapid and effective for any vessel layout (within rather rough limits of similarity). The mesh contained in the internal cylinder experiences a rigid movement (in this case a rigid rotation around the axis of the cylinder); said movement is propagated to the exterior thanks to the *RBF* centres, and is contained by the exterior cylinder where the *RBF* points are fixed, so that only the portion of mesh included between two cylinders will be deformed (Figure 10).

A complete morphing action takes approximately 80 s in serial and 35 s running on 4 cores (using hyper-threading mode on 2 physical cores). The mesh in question is relatively small (1.5 million nodes approx.), but in any case the method functions very effectively in parallel and can be utilised with meshes of hundreds of millions of cells within reasonable timeframes. For example, Cella & Biancolini (2012) have employed an RBF solver utilising a set-up of approximately 430,000 points to move a mesh composed of 14 million hexahedral cells (approximately 14 million nodes) resulting in 1,337 s for the RBF solving and 5,445 s to move the grid using a quad-core.

Using the aforementioned methodology, *AWA*s contained between 17° and 29° (absolute values) were tested. Table 3 shows the good quality indexes of the mesh deformed with this parameter.

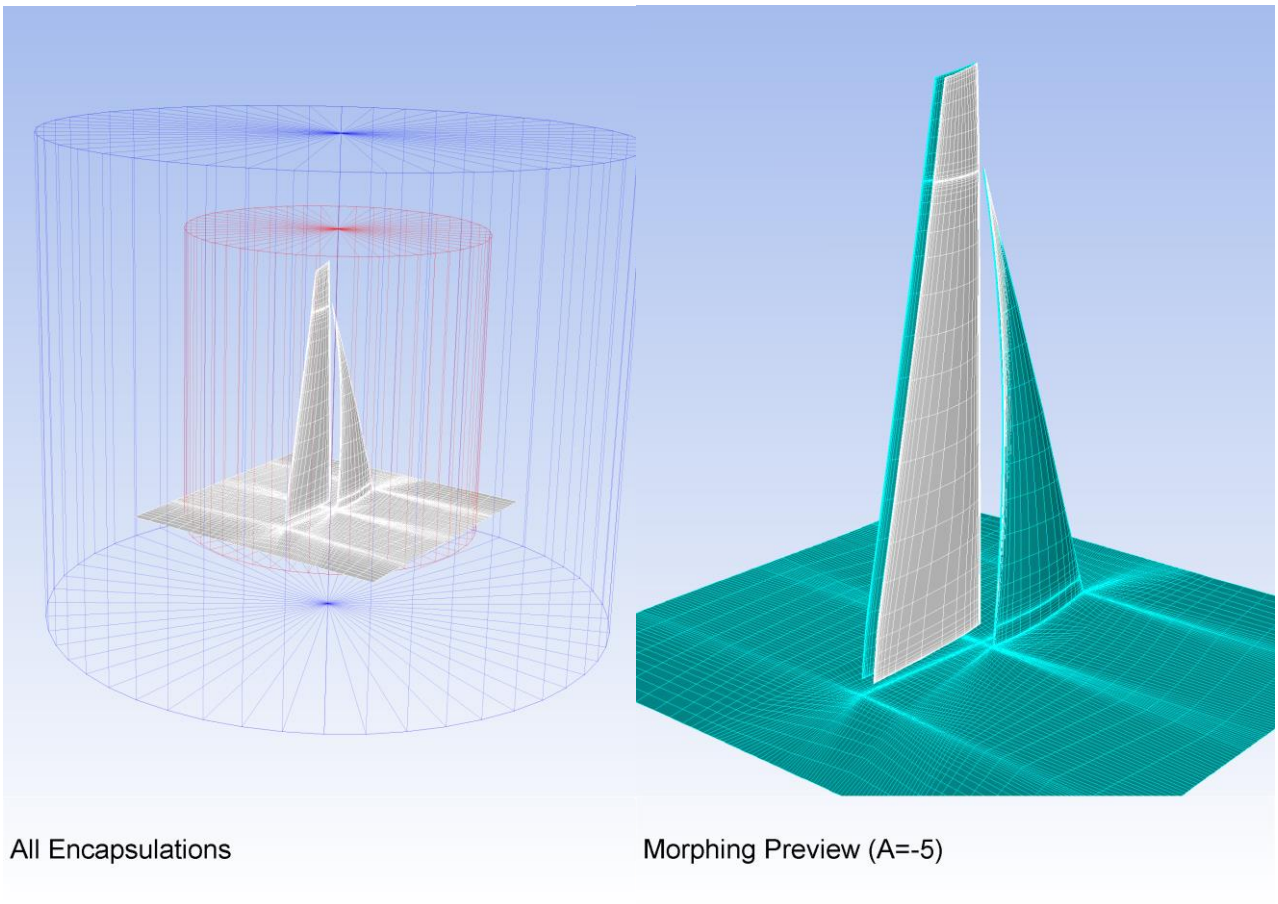


*Figure 10. Cylindircal encaps used to control the AWA (left) and deformation preview @ AWA = 5° (right).*

| ***AWA morphing amplification*** | ***minimum orthogonal quality*** | ***maximum aspect ratio*** |
|---|---|---|
| *-2* | *1.59e-02* | *1.562e+03* |
| *0* | *1.64e-02* | *1.555e+03* |
| *10* | *1.29e-02* | *1.571e+03* |

*Table 3. Quality of the deformed meshes calculated at the extreme values of the range explored for the AWA. (1 amplification unit = 1° deformation on the baseline).*

### *heeling angle*

The *heeling angle* presents more difficulties in its management, especially with this type of model in which the genoa intersects the floor. A first setup was defined imposing the desired rotations upon both the sails, leaving the portion of genoa contained between the section at zero height and the boom's height free to deform, furthermore assigning a null movement at all points upon the base plane; to complete the whole, a *domain encap* was utilised. The shape of the deformed sail thus obtained still did not appear satisfactory. It was therefore decided to improve the settings using a two-stage approach. In the first, the surface of the genoa is modelled by assigning a rigid rotation to the points in the upper section of the sail (allowing a certain degree of deformability); the points at the intersection of the sail and base plane are then fixed. The second stage, utilised for the deformation of the volume, requires a setting similar to the one utilised for the adjustment of the sails' *sheeting angle*, with the difference being the type of movement imposed. The mainsail rotates around the heeling angle and the genoa is rotated utilising the result of the first stage, which guarantees the desired shape being grafted onto the entire sail surface, including the deformable part (Figure 11).

The range of tested leeward heeling was set on -1°÷20°. Table 4 shows the quality analysis performed on the mesh morphed at the boundaries of the range of validity for the heeling angle. It is worth noting how the quality of the mesh geometry is substantially preserved although when reaching high levels of amplification, therefore when the portion of the mesh around the intersection between the genoa and the plate is particularly stressed.